Accepted manuscript, Gülcher et al. (2019), EPSL, 506:195-208, https://doi.org/10.1016/j.epsl.2018.10.042

Gülcher et al. (2019)

On the formation of oceanic detachment faults and their influence on intra-oceanic subduction initiation: 3D thermomechanical modeling

Earth and Planetary Science Letters, 506, 195-208

https://doi.org/10.1016/j.epsl.2018.10.042

Accepted manuscript, Gülcher et al. (2019), EPSL, 506:195-208, https://doi.org/10.1016/j.epsl.2018.10.042

On the formation of oceanic detachment faults and their influence on intra-oceanic subduction initiation: 3D thermomechanical modeling

Anna J. P. Gülcher * [1], Stéphane J. Beaussier [1], Taras V. Gerya [1]

[1] ETH Zürich, Department of Earth Sciences, Zürich, Switzerland, * anna.guelcher@erdw.ethz.ch

Extensional detachment faults, which have been widely documented in slow-spreading and ultraslow-spreading ridges on Earth, can effectively localize deformation due to their weakness. After the onset of oceanic closure, these weak oceanic detachments may directly control the nucleation of a subduction zone parallel to the former mid-ocean ridge, as is suggested for the Neotethys in Middle Jurassic times. So far, this hypothesis has only been tested by 2D numerical models, whereas the geometry of detachment faults is intrinsically three-dimensional. Here, we conducted a series of 3D numerical thermomechanical experiments in order to investigate the formation of detachment faults in slow oceanic spreading systems and their subsequent response upon inversion from oceanic spreading to convergence.

Numerical results show that during the oceanic spreading stage, the formation of detachment faults strongly depends on the magnitude of the healing rate of faulted rocks in the oceanic lithosphere, that reflects the stability of hydrated minerals along fractured rocks. The detachment faults formed in our 3D numerical models deviate from the "rolling hinge model" of oceanic detachment faulting where fault footwalls are rotated and oceanic core complexes are thereby formed. Our results accentuate that the controlling physical parameters for the development of oceanic core complexes and detachment faults can differ, and that their coupled development in nature remains a key target for future research.

Upon modelled transition to compression, previously formed asymmetric spreading patterns are prone to asymmetric inversion, where one oceanic plate thrusts under the other. Our results suggest that detachment faults accommodate significant amounts of shortening during the initiation of oceanic closure, but, in contrast to the previously proposed simple conceptual model, no direct inversion of a single detachment fault into an incipient subduction zone is observed. Instead, a widespread interaction of multiple detachment faults occurs after the onset of convergence. Ultimately, the nascent subduction zone

cuts through the base of several pre-existing detachment faults, thereby forming an initial accretionary wedge in the incipient fore-arc.

1. Introduction

Subduction occurring at multiple locations on Earth is considered to be a key driving process of the modern plate tectonic regime (e.g., Gurnis et al., 2004; Stern and Gerya, 2017). Despite its importance, many aspects of subduction remain poorly understood. One of the most unresolved and controversial challenges in current geodynamic research involves the initiation of subduction zones (e.g., Gurnis et al., 2004; Stern, 2004; Stern and Gerya, 2017 and references therein). Based on theoretical considerations and natural data, Stern (2004) proposed two major modes of subduction initiation: spontaneous (i.e., caused by forces originating at the subduction initiation site and not elsewhere) and induced (i.e., caused by ongoing plate motion, or changes in plate motion caused by changes in force balance away from the subduction initiation site). In the first mode, cold, old lithospheric plates sink spontaneously in the mantle under their own weight due to their inherent gravitational instability (Vlaar and Wortel, 1976; Stern, 2004). The dynamics of the latter subduction initiation mode are governed by the interaction of forces that drive and resist subduction. In order to initiate an induced subduction zone, the externally applied compressional forces must overcome the resistive forces, i.e. the plates' elastic resistance to bending and the frictional shear resistance at pre-existing fault zones (McKenzie, 1977; Matsumoto and Tomoda, 1983; Gurnis et al., 2004). This constraint has been resolved in some cases by former numerical studies, such as the induced initiation of intra-oceanic subduction zones along transform faults and fracture zones in rift systems (e.g. Matsumoto and Tomoda, 1983; Gurnis et al., 2004; Stern and Gerya, 2017 and references therein).

The majority of recently initiated subduction zones are intra-oceanic, stressing the importance of a proper understanding of the various processes leading to modern intra-oceanic subduction initiation (Gurnis et al., 2004; Stern and Gerya, 2017). One particular intra-oceanic subduction initiation mechanism that has received attention recently concerns the inversion of spreading ridges to trenches (e.g., Agard et

a,l,. 2015; Maffione et al., 2015; van Hinsbergen et al., 2015; Duretz et al., 2016). Ophiolites overlying metamorphic soles are commonly thought to be generated after subduction has started near a ridge (Wakabayashi and Dilek, 2003), yet intra-oceanic subduction initiation parallel and close to oceanic spreading ridges remains controversial. Although young and thin lithosphere adjacent to ridges could potentially be easily deformed, a young lithosphere might not be negatively buoyant enough to favor subduction (Cloos, 1993) and a ridge push force will oppose compression. It is therefore not clear how easy it is to initiate subduction in this geodynamic setting (e.g. Stern and Gerya., 2017 and references therein).

Based on geochemical, geological and paleomagnetic data, the Mirdita ophiolite (Albania) is interpreted as a supra-subduction zone ophiolite that formed in the Middle Jurassic in the western Neotethys parallel to and near a spreading center in a forearc during subduction infancy (Stern and Bloomer, 1992; Maffione et al., 2015). Together with geological and paleomagnetic observations, the geochemical signatures of the Mirdita ophiolite led to the interpretation that the subduction zone initiated along an oceanic detachment fault parallel to the spreading center (Bortolotti et al., 2013; van Hinsbergen et al., 2015). These observations were supported by 2D numerical experiments undertaken by Maffione et al. (2015), suggesting that subduction can initiate along oceanic detachment faults formed during seafloor spreading.

Oceanic detachment faults are long-lived normal faults exposed at the seafloor and have been documented in many slow and ultraslow-spreading systems (e.g. Dick et al., 2003; MacLeod et al., 2002, 2009; Escartin et al., 2008). They are often associated with compositionally and tectonically complex oceanic lithosphere. One of the most striking features are massifs in which lower crustal and upper mantle rocks are exhumed at the seafloor, better referred to as oceanic core complexes (e.g. Cann et al., 1997; Escartin et al., 2003; Smith et al., 2008). Detachment faults can cut the lithosphere up to a depth of 7-8 km (Escartin et al., 2008), which allows seawater to infiltrate to greater depths. Mantle lithosphere can rise up to shallower levels, resulting in greater hydrothermal alteration of the surrounding lower crust and mantle rock, modifying its texture and forming secondary hydrous minerals – such as serpentinite and talc (Boschi et al., 2006). As a result of the weakening effects of these hydrous minerals, detachment faults

are associated with a substantially decrease of the overall strength of the oceanic lithosphere (McLeod et al., 2002; Boschi et al., 2006), which may encourage the localization of plastic strain upon compression. Detachment faults are therefore a likely candidate for the initiation of subduction when compressional far-field forces are applied (Maffione et al., 2015).

The hypothesis of intra-oceanic subduction initiation controlled by detachment faults requires further testing. So far, this subduction initiation mechanism has only been investigated with 2D numerical models with a prescribed, rather than spontaneously formed, detachment fault (Maffione et al., 2015). Furthermore, the geometry of detachment faults in oceanic spreading systems is intrinsically three-dimensional, demanding a 3D modeling approach (e.g., Tucholke and Lin 1994; Escartin et al., 2003, 2008), whereas most previous explorations of faulting in extensional systems were done in 2D (e.g. Lavier et al., 1999; Huismans and Beaumont, 2002, 2003; Buck and Poliakov, 1998; Buck et al., 2005). Detachments represent relatively small structures in oceanic basins and it remains unclear how discrete detachments can link upon compression to form a continuous, wide subduction zone (Maffione et al., 2015). Thus, the formation and geometry of detachment faults in a three-dimensional slow-spreading oceanic basin as well as how detachments can initiate a self-sustaining subduction zone parallel to the ridge axis, are left unresolved.

In this paper, we conducted a series of 3D numerical thermomechanical experiments in order to investigate the formation of detachment faults in slow oceanic spreading systems and their subsequent response upon inversion from oceanic spreading to convergence. The research is divided into two main parts:

(i) Improve our understanding of the formation of detachment faults in (ultra)slow oceanic spreading systems in three-dimensions. What physical parameters control their 3D geometry and spatial distribution?

(ii) Investigate the response of a slow-spreading rift system with detachments upon compression. Under which conditions will subduction be initiated and how is the incipient subduction suture affected by the detachments?

2. Methods

2.1 Numerical approach

Numerical experiments were performed using the 3D thermomechanical I3ELVIS code (Gerya and Yuen, 2007; Gerya, 2013), based on a combination of a Finite-Difference method applied on a fully staggered Eulerian grid and a marker-in cell technique. The incompressible continuity equation, momentum equation and heat conservation equation are solved on the undeformed Eulerian grid. Material properties are advected on the moving Lagrangian markers.

2.2 Model set-up

The initial model set-up is shown in Figure 1 and corresponds to the onset of oceanic spreading within a young oceanic lithosphere with a 7-km thick crust. The Eulerian computational domain corresponds to a physical domain of 98x98x50 km resolved with a regular grid of 197x197x101 nodes. Six million Lagrangian markers are randomly distributed within the model domain. Material parameters used in the numerical experiments are shown in Table 1. The initial thermal structure of the lithosphere is defined according to the cooling profile of a semi-infinite half-space (Turcotte and Schubert, 2002) going outward on both sides of a thermal perturbation, localizing the ridge. This profile was determined according to the adopted spreading rate of each model. A constant temperature boundary condition of 0 °C and 1300 °C are used respectively at the top and bottom of the model.

Free slip boundary conditions are imposed on the front and back boundaries. The free surface boundary condition is approximated on top of the crust by defining a 5 km sticky water layer (Schmeling et al., 2008). A high thermal conductivity is used for the upper sticky water layers to ensure an efficient heat transfer at the upper surface of the plate. Spreading, and subsequent convergence, is assumed to be caused by far-field forces and apply on all rock types. Boundary conditions are constant symmetrical spreading rates in x-direction where $v_{spreading} = v_{xleft} + v_{xright}$ and $v_{xleft} = v_{xright}$ (see Fig. 2). Compensating vertical influx velocities which are constant along the whole upper and lower boundaries are derived from $v_x(t)$ to ensure conservation of model volume as well as constant average thickness of

the sticky water layer. Because detachment faults form in ultraslow to slow-spreading oceanic ridges (e.g. Dick et al., 2003; Smith et al., 2006), full spreading rates were taken in a limited range of 1.5 to 2.5 cm/yr, characteristic of ultraslow to slow-spreading systems (Dick et al., 2003). Inversion from divergence to convergence is implemented by a linear interpolation of the prescribed velocity boundary condition from divergence velocity v_{init} to convergence velocity v_{end} at each time step during a predefined transition time interval (t_{init}-t_{end}) in the following way:

$$v_x(t) = v_{init}(1-a) + v_{end} * a \text{ with } a = \frac{t-t_{init}}{(t_{init}-t_{end})} \quad (1)$$

Inversion is set to happen after 5 million years of oceanic spreading, such that a mature spreading pattern can first be formed at the ridge. The transition time from extension to compression was set to 3-5 Myr to allow for gradual changes in deformation.

2.3 Numerical implementations of oceanic spreading processes

In order to accurately model plate break-up and oceanic spreading, an implementation of the successive melting/accretion-related processes is required. The following key processes were suggested to be critical for this purpose: (i) thermal accretion of the oceanic mantle lithosphere resulting in plate thickening; (ii) partial melting of the asthenospheric mantle, melt extraction and percolation towards the ridge resulting in crustal growth; (iii) crystallization of the new oceanic crust beneath the ridge and (iv) hydrothermal circulation at the axis of the ridge resulting in excess cooling of the crust (e.g. Buck et al., 2005; Gregg et al., 2009; Katz, 2010). These processes are included in our numerical model in a simplified manner as described by Gerya (2013). It is important to note that the adopted magmatic model is designed to reproduce a gross-scale distribution of melt production processes below a ridge but cannot replicate the exact volcanic/magmatic activity, which is commonly observed around slow-spreading ridges in nature (Gerya, 2013).

2.4 Rheology

A constant, low viscosity of 10^{18} Pa s is implied for the partially molten crustal and mantle rocks, whereas a non-Newtonian visco-plastic rheology is implied for the lithospheric plates. Upper and lower

cut-off viscosity limits for the lithosphere were set to 10^{24} and 10^{18} Pa s. The viscous rheology contains both stress-independent diffusion creep and stress/strain-rate dependent dislocation creep (Ranalli, 1995). Brittle-plastic rheology of the plates assumes fracture-related strain weakening (e.g. Lavier et al., 2000; Huismans and Beaumont, 2002; Hieronymus, 2004; Gerya, 2013). This is implemented by using a Drucker-Prager yield criterion defining the visco-plastic transition:

$$\sigma_{II} \leq C + \varphi (P - P_f) \quad (2)$$

where σ_{II} is the second stress invariant (Pa), P is the dynamic pressure on solids (Pa), P_f is the hydrostatic fluid pressure ($P_f = \rho_f g y$ with ρ_f= 1000 kg/m^3, g=9.81 m/s^2 and y=vertical coordinate), C is the rock strength at $P - P_f = 0$ and φ is the internal friction angle coefficient. Strain weakening is obtained by strain-dependent linear interpolation between parameterized minimum and maximum values of C and φ :

$$\varphi = 1 \text{ when } P \leq P_f \text{ (tensile fracture)} \quad (3)$$

$$\varphi = 0.6\left(1 - \frac{\gamma}{\gamma_0}\right) \text{ for } \gamma \leq \gamma_0 \text{ and } \varphi = 0 \text{ for } \gamma \geq \gamma_0; P \geq P_f \text{ (confined fracture)} \quad (4)$$

$$C = C_0 + (C_1 - C_0)\frac{\gamma}{\gamma_0} \text{ for } \gamma \leq \gamma_0 \text{ and } C = C_1 \text{ for } \gamma \geq \gamma_0 \quad (5)$$

where C_0 and C_1 are the initial and final strength values for the fracture-related weakening, respectively. $\gamma \geq 0$ is the integrated plastic strain (with $\gamma_0 = 1$ as the upper strain limit for fracture related weakening) and is calculated via:

$$\gamma = \int \sqrt{\frac{1}{2}(\dot{\varepsilon}_{ij})^2}\, dt - \int \dot{\varepsilon}_{healing}\, dt \quad (6)$$

here, $\dot{\varepsilon}_{ij}$ is the plastic strain rate tensor and $\dot{\varepsilon}_{healing}$ is the fracture healing rate. Fracture-related weakening is therefore implemented as a linear interpolation from C_0 to C_1 and from φ=0.6 to φ=0 for $\gamma \leq \gamma_0$. This assumed strain weakening model is adopted from previous studies of mid-ocean ridges and can correspond to multiple mechanism of weakening such as formation of weak hydrated phases by fluid percolation (Escartin et al., 2003) and/or fault gouge formation (Huismans and Beaumont, 2002). The amount of strain weakening is mainly investigated in this study through the ratio of C_0 to C_1, hereafter termed as the cohesion ratio. An increase of cohesion ratio may represent a decrease in coherency of brittle material due to initial pressure-independent fracturing, and vice versa (Eq. (5); Allken et al., 2012;

Gerya, 2013). Partial strain healing of deactivated shear zones is applied by imposing a constant plastic healing rate $\dot{\varepsilon}_{healing}$ that reduces the accumulated plastic strain with time. When the second strain rate invariant $\frac{1}{2}(\dot{\varepsilon}_{ij})^2$ is greater than the plastic healing rate for $\dot{\varepsilon}_{healing}$, strain weakening occurs, whereas strain healing of the faults occurs when the second invariant is smaller than $\dot{\varepsilon}_{healing}$. Following former numerical investigations of spreading systems in 3D, magnitudes of the healing rate were taken in the range of 0 - 10^{-13} s^{-1} in the numerical experiments (from Gerya, 2013; Puthe and Gerya, 2014). In cases where $\dot{\varepsilon}_{healing}$ is set to zero, maximum weakening of fractured rocks occurs, and these models thereby represent spreading systems in which hydrated minerals are able to permanently weaken fractured rocks. The upper limit of $\dot{\varepsilon}_{healing}$= 10^{-13} s^{-1} reflects a fast healing of deactivated fractures, on the scale of geodynamic processes, which undergo no chemical change to a weaker phase (Lyakhovsky and Ben-Zion, 2008).

3. Numerical results

The conditions and results of the performed numerical experiments investigating spreading patterns and inversion are shown in table 2. In these experiments, different initial and boundary conditions were adopted: (i) spreading/inversion rates; (ii) inversion timing (iii) healing rate $\dot{\varepsilon}_{healing}$ and (iv) the cohesion ratio C_0/C_1 of solid rocks. The results of modeling of the 3D (ultra)slow oceanic spreading patterns and the responses of these spreading systems upon inversion will be discussed in the sections below.

3.1 Development of 3D oceanic spreading patterns

3.1.1 Reference model development

The evolution of the reference model (*diaa*) during 5 million years of oceanic spreading is presented in Figure 2. In this reference model, the healing rate was set to zero and the C_0/C_1 cohesion ratio to 10/3. The initial straight ridge produces two conjugate normal faults bounding half-grabens in the brittle lithosphere along which deformation localizes. Asymmetric accretion occurs as more motion is

accommodated by one of the two faults, which cuts deeper into the lithosphere and is more pronounced than the other (Fig. 2a). This detachment fault localizes a significant amount of extensional slip in its initial stage. Another inherent feature is that asymmetric accretion spontaneously varies along the ridge axis. The dip direction of the dominant detachment fault is abruptly reversed at z=75 km (Fig. 2a). This spontaneous sharp transition in asymmetric accretion is clearly visible on the bathymetry of the ocean floor and slightly offsets the ridge axis. This position for the polarity change is likely chosen randomly due to the presence of small random perturbations in the initial positions of rock markers.

The successive evolution (Figs. 2b-d) is characterized by the episodic formation of new detachment faults at the spreading ridge, which subsequently become less active and migrate away from the ridge. The lifetime of the active detachment faults is approximately 0.6 Myr and their vertical offset is 0.5-1.0 km. The migrating detachment faults accommodate less and less deformation whereas new, active detachment faults form at the ridge within the newly accreted crust. The result is a faulted crustal pattern in which the detachment faults, separated by 5-10 km, run approximatively parallel to the spreading ridge and where strain localization is evenly distributed over the migrated detachment faults. The detachment faults extend through a maximum length of 80 km and cut the lithosphere to depths of 7-8 km. The bathymetry profiles show alignments of ridge-parallel highs and lows. The topographic hills are separated by valleys created by the slip along the detachment faults. As new detachment faults are formed with continuous spreading, the deflection point at which sense of asymmetric accretion is reversed, migrates towards the origin of the z-axis along the ridge axis. At this position, the active detachment faults are slightly offset (Figs. 2b-d). This stepwise migration of fault offset point forms an oblique pattern with an ~ 50° angle to the ridge, which is visible in the bathymetric profiles (Fig. 2d). We refer to this bathymetric pattern as a 'Christmas tree pattern'.

Even though many detachment faults are formed, mantle rock is never exhumed up to the surface, and thus no oceanic core complexes are formed throughout the evolution of the model. This is because new detachment faults are formed closer to the ridge before the faults accumulate sufficient offset to exhume mantle rocks.

3.1.2 Influence of model parameters

Typical slow-spreading structures, such as asymmetric accretion and crustal faults, were obtained in most of the conducted experiments. Our results show that the mature oceanic spreading pattern is strongly affected by the healing rate and cohesion ratio (C_0/C_1) of faulted rocks. Most experiments were assigned a full spreading rate of 1.9 cm/yr, and results from numerical experiments with different spreading rate values show that, within the investigated range, the spreading rate has little effect on their formation and structure (table 2).

Figure 3 shows the mature spreading patterns of 12 numerical experiments with varying healing rates and cohesion ratios. Off-axis detachment faults and transforms are prominent in models with zero to very low ($\leq 10^{-15}$ s^{-1}) healing rates, representing greater weakening of fractured rocks, and with large cohesion ratios, representing less coherency in the rocks. In the reference model (Fig. 3a), many regular detachment faults are formed than run parallel to the ridge axis. Increasing the healing rate results in a smoother bathymetry and more symmetrical spreading pattern (Figs. 3a,d,g,j). Three different scenarios regarding the formation and evolution of detachment faults can be distinguished: (1) in models with $\dot{\varepsilon}_{healing} \leq 10^{-15}\ s^{-1}$, detachment faults are formed and preserved as oceanic spreading continues (Figs. 3a-f); (2) models with $\dot{\varepsilon}_{healing} = 10^{-14}\ s^{-1}$ show the formation of detachment faults near the spreading ridge which become completely abandoned as soon as they migrate outwards (Figs. 3g-i); (3) in models with $\dot{\varepsilon}_{healing} = 10^{-13}\ s^{-1}$, small- offset faults are formed on both sides of the ridge. In these cases the accretion is symmetrical, and the fault offset too small to be quantified (Figs. 3j-i). Therefore, we do not consider these faults as detachment faults.

Increasing the C_0/C_1 cohesion ratio produced models with fewer detachment faults, which have a larger variability in shape and length and are separated by a greater distance of 10 to 15 km (Figs. 3a-c). Irregularity of the ridge is also promoted by larger cohesion ratios, and segmentation of the ridge by ridge-perpendicular transform offsets occurs in the models combining large cohesion ratios with low healing rates (Figs. 3c,f).

3.2 Inversion of 3D oceanic spreading patterns

3.2.1 Reference model development

The evolution of the reference model (*diaa*) during inversion from spreading to convergence is presented in Figure 4. Inversion took place from 5-8 Myr. The mature spreading pattern after 5.0 million years of spreading is shown in Figure 4a. Many detachment faults up to 80 km long run parallel to the spreading ridge and localize extensional deformation. As the spreading rate decreases during the initial stage of inversion, the temperature decreases near the ridge, leading to lithospheric thickening (Fig. 4b). Just after plate motion is inverted to convergence (Fig. 4c), detachment faults adjacent to the spreading ridge on both sides become reactivated as reverse faults. With time, the reactivated detachment faults located on the right-hand side of the former ridge starts to accommodate most of the shortening, leading to the initialization of a thrusting of one of the oceanic plates under the other. With further convergence, the downgoing plate penetrates further into the mantle, and the surface trace of the underthrust retreats (Figs. 4c-e). The main thrust cuts through the base of several detachments at one side of the ridge and former detachment faults reactivate as back-thrust atop the downgoing plate. This forms an accretionary wedge-like structure from the dismembering of the overriding plate. After 1 million years of constant convergence with velocity v_{end} (Eq. 1), the underthrusting pattern becomes well defined (Fig. 4e). One of the oceanic lithospheric plates is further thrusted under the other, but the deep part of the thrust becomes almost horizontal. Deformation is mainly accommodated along the reactivated detachment faults, which interact with one another within a nascent accretionary wedge. The relatively narrow high-resolution models cannot be used to further investigate the incipient subduction as the retreating trench starts to interact with one of the lateral boundaries (Fig. 4e).

3.2.2 Influence of model parameters

The inversion results at time t=9.0 Myr for models with different $\dot{\varepsilon}_{healing}$ values are shown in Figure 5. Symmetrical responses upon compression are encouraged by a large healing rate of 10^{-13} s^{-1}: upon inversion, the model *diac* with an initially symmetrical, smooth spreading pattern shows two active conjugate thrusts formed on both sides of the spreading ridge. The ridge swell forms atop the original spreading ridge and evolves in a symmetrical pattern. In the three other models with lower fracture

healing rates, an asymmetrical pattern with underthrusting forms. As follows from the comparison of these three models, an increase in fracture healing rate does not change the mechanism of formation but influences the geometry of the accretionary wedge-like structure and the morphology of the thrust. The pre-existence of regularly spaced deep detachment faults (models *diaa* and *diad,* Figs. 5a,b) encourages a stable horizontal underthrust associated with an accretionary wedge in which the detachments faults interact with one another to form back-thrusts. Without the presence of such detachment faults (model *diab*, Fig. 5c), the downgoing plate plunges directly into the mantle at a steeper angle and no evident accretionary wedge forms.

Figure 6 shows the inversion results at time t=9.0 ma for models with different cohesion ratios (C_0/C_1). All models yielded underthrusting of one plate along a major reverse fault. Increased cohesion ratios produce larger amount of localized deformation along the main thrust plane and a smaller accretionary wedge atop the fault (Figs. 6a-c).

4. Discussion

4.1 Detachment faults in slow-spreading systems

Detachment faults and off-axis strain localization have been documented in many of the conducted experiments. In our 3D models, oceanic spreading geometries have shown to have a significant dependence on the value of the healing rate $\dot{\varepsilon}_{healing}$ of fractured rocks and cohesion ratio $C_0/\ C_1$, as illustrated in Figure 3. The numerical results indicate that the formation and preservation of detachment faults in oceanic slow-spreading systems are mainly promoted by low to zero healing rates ($\dot{\varepsilon}_{healing} \leq 10^{-15}$ s^{-1}). The low healing rate would correspond to hydration of the fault zone through fluid infiltration, which is unlikely to heal (dehydrate) during seafloor spreading and subduction initiation (Escartin et al., 2003). Detachment faults formed in our models cut the lithosphere to depths of 7-8, which would allow for hydration along the fault zone (Escartin et al., 2008) and thereby the results are consistent with this suggested relationship between low healing rates and hydrothermal alteration of fractured rocks. The

pressure- independent fracture weakening (i.e. cohesion ratio), mainly affects the geometry and spacing of the detachment faults but not their presence or absence in spreading patterns (Fig. 3).

Oceanic spreading models with ample healing of fractured rocks are inherently symmetric (Figs. 3j-l) whereas increased strain weakening breaks this symmetry and promotes asymmetric accretion. (Figs. 3a-i). The positive feedback between strength reduction and increased strain, leading to further weakening of fractured rocks, and its direct correlation with the development of asymmetric extensional systems was acknowledged in former 2D numerical studies (e.g. Huismans and Beaumont, 2002, 2003) and is endorsed by our 3D results. The lifetime of faults is also greatly affected by weakening of fractured rocks: increasing the healing of fractured rocks decreases the average lifetime of faults and vice versa (Puthe and Gerya, 2014), which is encouraged by our models in which the lifetime of detachment faults decreases from 0.6 Myr in the reference model (*diaa*, Figs. 2; 3a) to zero when the healing rate is too large to maintained long-lived weakening of the lithosphere (models *diad, diap, diat;* Figs. 4j-l). The influence of the coherency of the rock, i.e. the cohesion ratio, in our 3D numerical models are consistent to former 2D numerical studies of extensional faulting in two ways: (i) the correlation of a larger cohesion drop, i.e. cohesion ratio, and greater normal fault offsets (Buck et al., 1998; Lavier et al., 1999; Huismans and Beaumont, 2003), and (ii) larger spacing between normal faults for models with greater cohesion ratios (Huismans and Beaumont, 2003). The third dimension of our models reveals that numerical experiments with an increased cohesion ratio are more prone to transformal offsets, in addition to wider spacing of detachment faults. The evolutionary sequence of detachment fault formation and migration away from the ridge also agrees with previous 3D numerical studies of (ultra)slow oceanic spreading systems (Puthe and Gerya, 2014). Yet, the displacement accommodated along the detachment faults is typically moderate, and these structures do not exhume mantle rock to the surface. This faulting geometry deviates from the “rolling hinge” model of detachment faulting (Lavier et al., 1999), in which detachment faults initiate as steeply dipping normal faults but then rotate to shallower dip as a result of flexure in the footwall. It is suggested that the development of long-lived, low-angle detachment faults and accompanying oceanic core complexes require that a small part (~30-50%) of the total extension is accommodated by magmatic dyke accretion while the rest is accommodated by lithosphere thinning (e.g. Buck et al., 2005; Behn and Ito, 2008; Tucholke et al., 2008). As our model does not account for any dyke-

related processes, the entire oceanic crust is accreted by the cooling of the roof and the walls of a large shallow magma reservoir that forms spontaneously under the ridge as the result of melt extraction from the mantle (Gerya, 2013). Our numerical set-up thereby deviates notably from the previous 2D models, which could explain the observed difference in detachment fault geometries in numerical results.

The three-dimensionality of our models does provide a fascinating new aspect to slow-spreading systems. The "Christmas tree" bathymetric pattern, generated consistently in many of the numerical experiments (Fig. 3), and represent variation along the ridge in asymmetric accretion, expressed as a reversal in the dip direction of active detachment faults. The patterns require asymmetrical accretion along a bended ridge, and are thereby created in models with low healing rate values ($\dot{\varepsilon}_{healing} \leq 10^{-15}$ s^{-1}) and relative low cohesion ratios ($C_0/C_1 = 10/3$).

4.2 Comparison of oceanic spreading models with natural data

Several common features of natural oceanic spreading systems have been reproduced numerically in this study. Orthogonal ridge-transform patterns are common in slow oceanic spreading ridges on Earth (e.g. Gerya, 2013 and references therein) and are formed spontaneously in several of our experiments (models *diam, diaq, dian, diar*; Figs. 3b-f). The "Christmas tree" bathymetric pattern (oblique patterns ~50° to the spreading ridge offsetting detachment faults) is systematically generated in the remaining part of the numerical experiments that accrete in an asymmetrical way (Fig. 3). Although the exact physics behind its development remains to be explored, the characteristic pattern also has analogous observations on spreading systems on Earth. Similarities between natural observations and several numerical models are shown in Figure 7. The ridge-oblique bathymetric patterns are observed in e.g. (a) the slow-spreading Mid-Atlantic ridge near 22° (McDuff and Heath, 2001); (b) the Carlsberg Ridge, Arabian Sea (Kattoju et al., 2015).

Most of the experiments show rough topographies with highs and lows running parallel to the ridge-axis. These structures are very similar to abyssal hills, one of the most prominent features of slow-spreading mid-ocean ridge flanks (Buck et al., 2005). The abyssal hill topographic pattern is interpreted as a product of extensional faulting at slow mid-ocean ridges and has been mapped in many places on Earth.

Buck et al., (1998; 2005) showed the occurrence of these patterns in several locations on the Mid Atlantic Ridge and the Southeast Indian Ridge. From these bathymetric profiles, an average separation between abyssal hills of 5-7 km was measured. This wavelength agrees with the average distance between the detachment faults generated in the numerical models with abundant weakening of rocks at low cohesion ratios (Figs. 3a and d).

4.3 Ridge inversion

Numerical results shown in Figure 5 indicate that (ultra)slow-spreading ridges with asymmetrical faulting patterns manifested by the presence of deep detachment faults are prone to develop subduction-like underthrusting when ridge-perpendicular compressional forces are applied. Inversion of the spreading models show that underthrusting never localizes at the spreading ridge, but instead at one of the pre-existing detachment faults, and to that extend endorse the findings by numerical explorations by Maffione et al. (2015). Yet, none of our 3D experiments showed the direct inversion of a single detachment fault into an incipient subduction zone (as proposed by Maffione et al., 2015). The suboptimal orientation of the reactivated detachment fault (i.e. steep dip angle and limited lateral extent along the ridge) prevents direct plunging of the down-going plate along this single detachment fault. Instead, the thrust plane choses a lower angle geometry and thereby cuts through the base of several former detachment faults which interact with one another to form an accretionary wedge-like structure (Fig. 4e). Also, in the absence of exhumed mantle rock that forms an oceanic core complex in the footwall, the gravity anomaly of the underthrusted lithosphere is insufficient to induce a bending of the oceanic lithosphere. This explains why the down-going lithosphere is underplated below overriding plate and stagnates around 20 km depth.

Although the numerical models do not allow for the development of a full-fledge subduction zone, they can be partially correlated with the geological record of ophiolites in Albania and Greece (Bortolotti et al., 2013). For simplicity we will only discuss correlations with the Mirdita ophiolite as the mechanism of near-ridge subduction initiation through detachment fault inversion was based on this ophiolite only (Maffione et al., 2015 and references therein). A major argument in favor of the validity of the models in this study

is that they reproduce the high peak pressure-temperature conditions recorded in the metamorphic sole at the time of subduction initiation (624°C to 769°C with pressure <0.7 GPa; Gaggero, 2009) as well as the inverted metamorphic gradient (assuming that the base of the hanging wall in the model corresponds to the metamorphic sole; Fig. 4). In many of the numerical experiments, the downgoing plate is very fragmented during oceanic closure, thereby forming an accretionary wedge atop the main thrust mainly composed of oceanic lithospheric fragments (Figs. 5a-b). This fragmented prism cannot be observed in the Mirdita ophiolite or in the Melange below, which is dominated by sedimentary fragments from the Adria continental margin (Bortolotti et al., 2013), but it is likely that these fragments have disappeared through the process of subduction erosion by the time of obduction and that only a few remnants are preserved in the mélange below the ophiolite. Lastly, there are significant differences in the way the detachment faults are reactivated in the numerical models and the geological record of the Mirdita ophiolite. In our results, it is the detachment fault closest to the ridge that is reactivated during compression (Fig. 4). The Mirdita ophiolite contains a fossil detachment fault that is interpreted as closer to the ridge but not reactivated during subduction initiation (Maffione et al., 2013). This discrepancy might be because, unlike in nature (Maffione et al., 2013), the detachment faults in our model are short-lived and do not form large-slip detachments that expose oceanic core complexes (e.g. Lavier et al., 1999). Large-slip detachment faults might be weaker (e.g. more strain weakening) and reach deeper in the lithosphere and therefore will be more likely to reactivate in inversion (Buiter et al., 2009) than short and steep detachment faults closer to the ridge. More studies would be necessary to properly elude this question. In particular, taking into account many similarities between naturally observed and numerically reproduced oceanic spreading patterns, our simulated ridge inversion patterns with an accretionary prism composed of multiple seafloor fragments should be of rather broad significance and call for further numerical studies and systematic comparison with other known ophiolite complexes worldwide (e.g., Vaughan and Scarrow, 2003).

4.4 Limitations and outlook

It is important to note that our numerical experiments were performed on a relatively small spatial scale with a high resolution and a simple geometry, aiming to form an initial basis for large-scale formation and inversion of complex spreading systems in 3D. Due to the model dimensions, we are limited in our ability to correlate our relatively small-scale and short-term ridge inversion models to geological observation in ophiolites. Also, the amount of induced plate convergence (<50 km) in the numerical models does not span the entire period of subduction initiation (e.g. Stern and Gerya, 2017 and references therein). Therefore, further high-resolution 3D numerical experiments investigating larger segments of an oceanic spreading system and the underlying mantle are still needed to develop a better understanding of detachment fault-controlled subduction initiation.

Our results emphasize the influence of the healing and weakening mechanisms occurring in faulted rocks on oceanic spreading patterns. It must be noted that the employed simplified strain weakening/healing model does not directly reflect the physics involved in the various weakening/healing processes, such as fluid percolation, hydration reactions and grain damage or growth. As fluid-rock interactions are greatly associated with detachment tectonics (e.g. Escartin et al., 2008), further theoretical development and numerical implementation of a more sophisticated and realistic lithospheric weakening/healing model might bring a better understanding of the relation between detachment faults, oceanic core complexes and subduction initiation.

5. Conclusions

We performed high-resolution three-dimensional numerical modeling of (ultra)slow oceanic spreading systems with detachment faults and their response upon subsequent ridge-perpendicular convergence.

Our numerical models suggest that asymmetric spreading and detachment fault development is mainly controlled by the low fracture healing rates of brittle/plastic lithospheric rocks. This low fracture healing rate reflects ample strain weakening along faults, possibly driven by hydrothermal alteration of

the fractured rocks. The modeled spreading patterns share key features with former 2D and 3D numerical studies as well as natural systems, such as asymmetrical rift development, ridge-parallel abyssal hills and transformal offsets. Numerical results deviate from the simple conceptual "rolling hinge" model of oceanic detachment faulting, where a long-lived main detachment fault is intrinsically associated with the development of an oceanic core complex (Lavier et al., 1999). Instead, detachment faults are regularly spaced and have moderate offsets. The melt supply by dykes in the spreading systems has not been assessed in this study, and we propose that in the future studies the magmatic vs. tectonic extension ratio should be coupled with the fracture weakening/healing parameters, to improve our understanding of extensional faulting behavior in slow-spreading systems.

Upon ridge-perpendicular convergence, the pre-existing detachment faults have been shown to localize extensive deformation. Our results indicate that asymmetric spreading patterns with multiple detachment faults are prone to asymmetric inversion, where underthrusting of one oceanic plate under the other occurs. Instead of a single detachment faults directly inverting into an incipient subduction zone, multiple ridge-parallel detachment faults interact with one another upon compression. The main thrust plane cuts through the base of several detachment faults, thereby forming an incipient accretionary wedge in the incipient fore-arc.

The formation of a continuous, self-sustaining subduction zone parallel to a pre-existing mid-ocean ridge remains an outstanding large-scale three-dimensional problem and future numerical modeling research is needed to account for larger spatial and temporal scales. Key targets for future three-dimensional modeling is (i) understanding the formation of and coupling between detachment faults and oceanic core complexes in slow-spreading systems, possibly by assessing both the melt supply as the healing/weakening parameters; and (ii) the effect of detachment faults on the initiation of a self-sustaining, laterally continuous subduction zone.

6. Acknowledgements

We thank M. Maffione and B. Kaus for their constructive comments and suggestions for this manuscript. All simulations were performed on the ETH-Zürich Brutus and Euler clusters. The open-source

software Paraview (http://www.paraview.org) was used for visualization of the data. We acknowledge support from the ERC ITN-grants CREEP and SUBITOP and the SNF projects Swiss-AlpArray and number 200020_169880.

7. References

Agard P., L. Jolivet, B. Vrielynck, E. Burov, P. Monie (2007) Plate acceleration: the obduction trigger? Earth Planet. Sci. Lett., 258: 428-441.

Allken, V., R. S. Huismans, and C. Thieulot (2012), Factors controlling the mode of rift interaction in brittle-ductile coupled systems: A 3D numerical study, Geochem. Geophys. Geosyst., 13, Q05010, DOI:10.1029/2012GC004077.

Behn, M.D., Ito, G., 2008. Magmatic and tectonic extension at mid-ocean ridges: 1. Controls on fault characteristics. Geochem. Geophys. Geosyst. 9(8), Q08010. DOI:10.1029/2008GC001965

Bortolotti, V., M. Chiari, M. Marroni, L. Pandolfi, G. Principi, and E. Saccani (2013), Geodynamic evolution of ophiolites from Albania and Greece (Dinaric-Hellenic belt): One, two, or more oceanic basins? Int. J. Earth Sci., 102: 783–811.

Boschi, C., G. L. Früh-Green, A. Delacour, J. A. Karson, and D. S. Kelley (2006), Mass transfer and fluid flow during detachment faulting and development of an oceanic core complex, Atlantis Massif (MAR 308N), Geochem. Geophys. Geosyst., 7, Q01004, DOI:10.1029/2005GC001074.

Buck, W. R. and Poliakov, A. N. B. (1998). Abyssal hills formed by stretching oceanic lithosphere. Nature, 392: 272-275, DOI:10.1038/32636

Buck, W. R., Lavier, L., and Poliakoc, A. N. B. (2005). Modes of normal faulting at mid-ocean ridges. Nature, 434: 719-723, DOI: 10.1038/nature03358

Buiter, S.J.H., Pfiffner, O.A., Beaumont, C., 2009. Inversion of extensional sedimentary basins: A numerical evaluation of the localisation of shortening. Earth Planet. Sci. Lett. 288, 492–504. doi:10.1016/J.EPSL.2009.10.011

Cann, J. R., Blackman, D. K., Smith, D. K., McAllister, E., Janssen, B., Mello, S., Avgerinos, E., Pascoe, A. R., and Escartin, J. (1997). Corrugated slip surfaces formed at ridge-transform intersections on the Mid-Atlantic Ridge. Nature, 385(23): 329-332, DOI: 10.1038/385329a0

Cloos, M., 1993. Lithospheric Buoyancy and Collisional Orogenesis - Subduction of Oceanic Plateaus, Continental Margins, Island Arcs, Spreading Ridges, and Seamounts, Geol. Soc. Am. Bull., 105: 715-737 DOI: https://doi.org/10.1130/0016-7606(1993)105<0715:LBACOS>2.3.CO;2

Dick, H. J. B., J. Lin, and H. Schouten (2003), An ultraslow-spreading class of ocean ridge, Nature, 426, 405–412. DOI: 10.1038/nature02128

Duretz, T., Agard, P., Yamato, P., Ducassou, D., Burov, E.B. and Gerya, T.V. (2016) Thermo-mechanical modeling of the obduction process based on the Oman Ophiolite case. Gondwana Res., 32: 1-10. DOI: https://doi.org/10.1016/j.gr.2015.02.002

Escartin, J., C. Mével, C. J. McLeod, and A. M. McCaig (2003). Constraints on deformation conditions and the origin of oceanic detachments: The Mid-Atlantic Ridge core complex at 15°45'N, Geochem. Geophys. Geosyst., 4(8), 1067, DOI:10.1029/2002GC000472

Escartin, J., Smith, D. K., Cann, J., Schouten, H., Langmuir, C. H., and Escrig, S. (2008). Central role of detachment faults in accretion of slow-spreading oceanic lithosphere. Nature, 455(7): 90-794. DOI:10.1038/nature07333

Gaggero, L., Marroni, M., Pandolfi, L., and Buzzi, . (2009). Modeling the oceanic lithosphere obduction: Constraints from the metamorphic sole of Mirdita ophiolites (northern Albania). Ofioliti, 34: 17-42.

Gerya, T. V., and Yuen, D. A. (2007). Robust characteristics methods for modeling multiphase viscoelasto- plastic thermo-mechanical problems. Physics of the Earth and Planetary Interiors, 163: 83-105. DOI: 10.1016/j.pepi.2007.04.015

Gerya, T. V. (2013). Three-dimensional thermomechanical modeling of oceanic spreading initiation and evolution. Physics of the Earth and Planetary Interiors, 214: 35-52. DOI: 10.1016/j.pepi.2012.10.007

Gregg, P. M., Behn, M. D., Lin, J., and Grove, T. L. (2009). Melt generation, crystallization, and extraction beneath segmented oceanic transform faults. Journal of Geophysical Research, 114, B11102. DOI: 10.1029/2008JB006100

Gurnis, M., Hall, C., and Lavier, L. (2004). Evolving force balance during incipient subduction. Geochemistry, Geophysics, Geosystems, 5(7). DOI: 10.1029/2003GC000681

Hall, C. E., Gurnis, M., Sdrolias, M., Lavier, L. L., and Müller, R. D. (2003). Catastrophic initiation of subduction following forced convergence across fracture zones. Earth and Planetary Science Letters, 212(1-2):15-30. Doi: 10.1016/S0012-821X(03)00242-5

Hieronymus, C. F. (2004). Control on seafloor spreading geometries by stress- and strain- induced lithospheric weakening. Earth and Planetary Science Letters, 222: 177-189. DOI: 10.1016/j.epsl.2004.02.022

van Hinsbergen, D. J. J., Peters, K., Maffione, M., Spakman, W., Guilmette, C., Thieulot, C., Plümper, O., Gürer, D., Brouwer, F. M., Aldanmaz, E. and Kaymakcı, N. (2015). Dynamics of intraoceanic subduction initiation: 2. Suprasubduction zone ophiolite formation and metamorphic sole exhumation in context of absolute plate motions. Geochemistry Geophysics Geosystems, 18: 1771-1785. DOI: 10.1002/2015GC005745.

Huismans, R. S. and Beaumont, C. (2002). Asymmetric lithospheric extension: the role of frictional plastic strain softening inferred from numerical experiments. Geology, 30: 211-214. DOI: https://doi.org/10.1130/0091-7613(2002)030<0211:ALETRO>2.0.CO;2

Huismans, S. R., & Beaumont, C. (2003). Symmetric and asymmetric lithopheric extension: Relative effects of frictional-plastic and viscous strain softening. Journal of Geophysical Research, 108(B10), 2496. https://doi.org/10.1029/2002JB002026

Kattoju, K. A., Mudholkar, A. and Samudrala, K. (2015). Slow Spreading Ridges of the Indian Ocean: An Overview of Marine Geophysical Investigations. The Journal of Indian Geophysical Union, 19(2): 137-159.

Katz, R. F. (2010). Porosity-driven convection and asymmetry beneath mid-ocean ridges. Geochemistry Geophysics Geosystems, 11, Q0AC07. , doi:10.1029/2010GC003282

Lavier, L.L., Buck, W.R., and Poliakov, A.N.B. (1999) Self-consistent rolling-hinge model for the evolution of large-offset low-angle normal faults: Geology, 27: 1127–1130. DOI: https://doi.org/10.1130/0091-7613(1999)027<1127:SCRHMF>2.3.CO;2

Lavier, L. L., Buck, W. R., and Poliakov, A. N. B. (2000). Factors controlling normal fault offset in an ideal brittle layer. Journal of Geophysical Research, 105: 23431-23442. DOI: 10.1029/2000JB900108

Lyakhovsky, V.D., & Ben-Zion, Y. (2008). Scaling relations of earthquakes and aseismic deformation in a damage rheology model. Geophysical Journal International 172(2): 651-662 https://doi.org/10.1111/j.1365-246X.2007.03652.x

McLeod, C. J., Escartin, J., Banerji, D., Banks, G. J., Gleeson, M., Irving, D. H. B., Lilly, R. M., McCaig, A. M., Niu, Y., Allerton, S., and Smith, D. K. (2002). Direct geological evidence for oceanic detachment faulting: The Mid-Atlantic Ridge, 15°45°N. Geology, 30: 879-882. DOI: 10.1130/0091-7613(2002)030<0879:DGEFOD>2.0.CO;2

McLeod, C. J., Searle, R. C., Murton, B. J., Casey, J. F., Mallows, C., Unsworth, S. C., Achenbach, K. L., and Harris, M. (2009). Life cycle of oceanic core complexes. Earth and Planetary Science Letters, 287:333-344. doi:10.1016/j.epsl.2009.08.016

Maffione M., Morris, A., Anderson, M.W. (2013). Recognizing detachment-mode seafloor spreading in the deep geological past. Scientific Reports 3, 2336; DOI:10.1038/srep02336

Maffione, M, Thieulot, C., van Hinsbergen, D., Morris, A., Plumper, O., and Spakman, W. (2015). Dynamics of intraoceanic subduction initiation: 1. Oceanic detachment fault inversion and the formation of supra-subduction zone ophiolites. Geochemistry Geophysics Geosystems, 18: 1541-1576. doi:10.1002/2015GC005746.

Matsumoto, M. and Tomoda, Y. (1983). Numerical-simulation of the initiation of subduction a the fracture-zone. Journal of Physics of the Earth, 31:183-194. DOI: http://doi.org/10.4294/jpe1952.31.183

McDuff, R. and Heath, G. (2001). Oceanography: Marine Geological Processes The school of Oceanography, University of Washington. Retrieved from http://www2.ocean.washington.edu/oc540/lec01-1/.

McKenzie, D.P., 1977. The initiation of trenches: a finite amplitude instability. In: Talwani, M., Pittman, W.C. (Eds.), Island Arcs, Deep Sea Trenches, and Back-Arc Basins. Maurice Ewing Ser. I. AGU, Washington, D.C., pp. 57–61.

Puthe, C. and Gerya, T. (2014). Dependence of mid-ocean ridge morphology on spreading rate in numerical 3-D models. Gondwana Research, 25:270-283. https://doi.org/10.1016/j.gr.2013.04.005

Ranalli, G. (1995). Rheology of the Earth. Chapman and Hall, London, UK.

Schmeling, H., Babeyko, A. Y., Enns, A., Faccenna, C., Funiciello, F., Gerya, T., Golabek, G. J., Grigull, S., Kaus, B. J. P., Morra, G., Schmalholz, S. M. and van Hunen, J. (2008). A Benchmark comparison of spontaneous subduction models - towards a free surface.. Physics of the Earth and Planetary Interiors, 171: 198-223. Doi: 10.1016/j.pepi.2008.06.028

Smith, D. K., Cann, J. R., and Escartin, J. (2006). Widespread active detachment faulting and core complex formation near 13 N on the Mid-Atlantic Ridge. Nature, 442:440-443. DOI: 10.1038/nature04950

Smith, D. K., Escartin, J., Schouten, H., and Cann, J. R. (2008). Fault rotation and core complex formation: Significant processes in seafloor formation at slow-spreading mid-ocean ridges (Mid-Atlantic Ridge, 13°–15°N), Geochem. Geophys. Geosyst., 9, Q03003, doi:10.1029/2007GC001699.

Stern, R. J. (2004). Subduction initiation: Spontaneous and induced. Earth and Planetary Science Letters, 226:275-292. doi: 10.1016/j.epsl.2004.08.007

Stern, R. J. and Bloomer, S. H. (1992). Subduction zone infancy: Examples from the Eocene Izu-Bonin-Mariana and Jurassic California arcs. Geological Society of America Bulletin, 104: 1621-1636. DOI: https://doi.org/10.1130/0016-7606(1992)104<1621:SZIEFT>2.3.CO;2

Stern, R.J., Gerya, T. (2017) Subduction initiation in nature and models: A review.

Tectonophysics, DOI: https://doi.org/10.1016/j.tecto.2017.10.014

Tucholke, B.E., and Lin, J., 1994, A geological model for the structure of ridge segments in slow spreading ocean crust: Journal of Geophysical Research, v. 99, p. 11,937–11,958, DOI: https://doi.org/10.1029/94JB00338

Tucholke, B. E., Behn, M. D., Buck, W. R., and Lin, J. (2008). Role of melt supply in oceanic detachment faulting and formation of megamullions. Geology, 36(6):455-458. DOI: https://doi.org/10.1130/G24639A.1

Turcotte, D. L. and Schubert, G. (2002). Geodynamics. Cambridge University Press, Cambridge.

Vaughan, A.P.M., and Scarrow, J.H. (2003). Ophiolite obduction pulses as a proxy indicator of superplume events?: Earth and Planetary Science Letters, v. 213, p. 407–416. DOI: 10.1016/S0012-821X(03)00330-3.

Vlaar, N. J. and Wortel, M. J. R. (1976). Lithospheric aging instability and subduction. Tectonophysics, 32: 331-351. DOI: https://doi.org/10.1016/0040-1951(76)90068-8

Wakabayashi J. Dilek Y., 2003, What constitutes "emplacement" of an ophiolite?: Mechanisms and relationship to subduction initiation and formation of metamorphic soles, in Dilek Y. Robinson P.T., eds., Ophiolites in Earth History: Geological Society of London Special Publication 218, p. 427–448. DOI: 10.1144/GSL.SP.2003.218.01.22

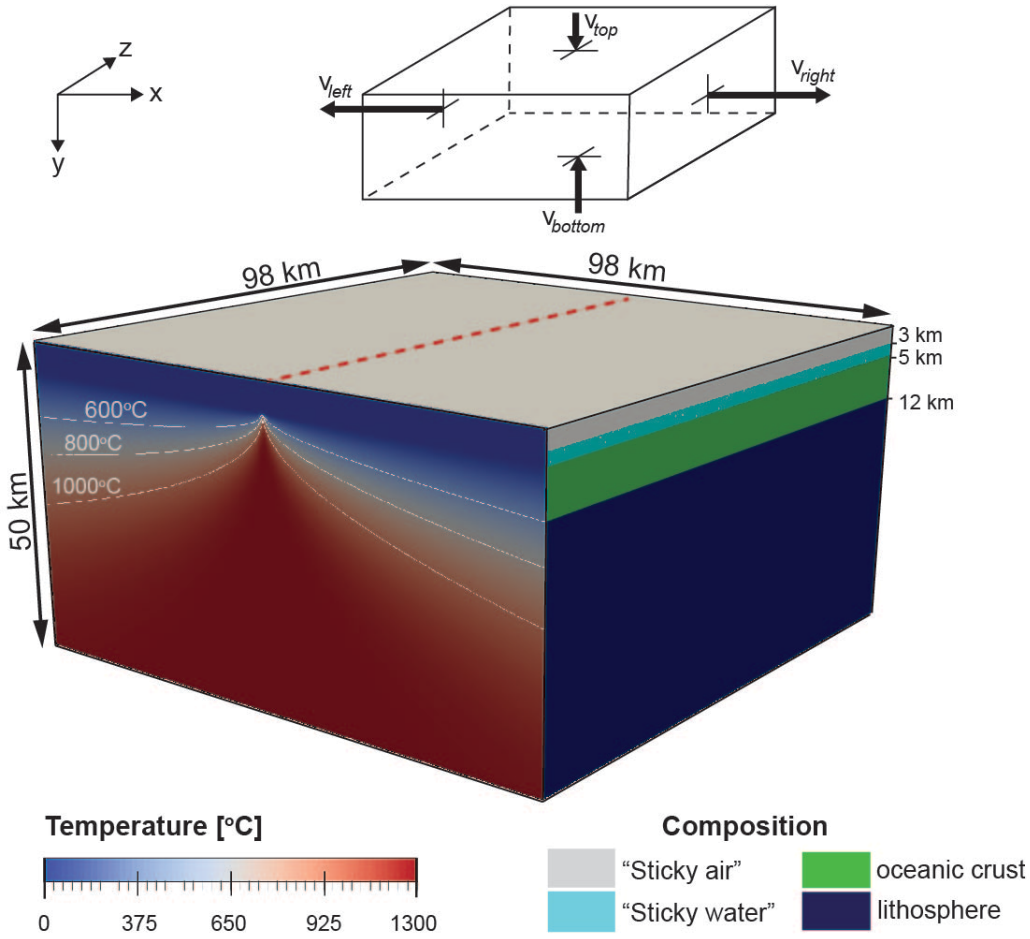

Figure 1 - Initial model set up and boundary conditions for 3D thermomechanical numerical experiments. The front side displays the thermal distribution, which is defined according to the cooling profile of a semi-infinite half-space (Turcotte and Schubert, 2002). On the right side, the material composition distribution is displayed. An oceanic crust of 7 km overlies the lithosphere. Boundary conditions are constant spreading rate in x direction and compensating vertical influx velocities through the upper and lower boundaries. Free slip is assigned to the front and back boundaries in the x-y plane. A free surface is implemented by imposing a "sticky" water and air layer on top (Schmeling et al., 2008). Velocity box adopted from Gerya (2013).

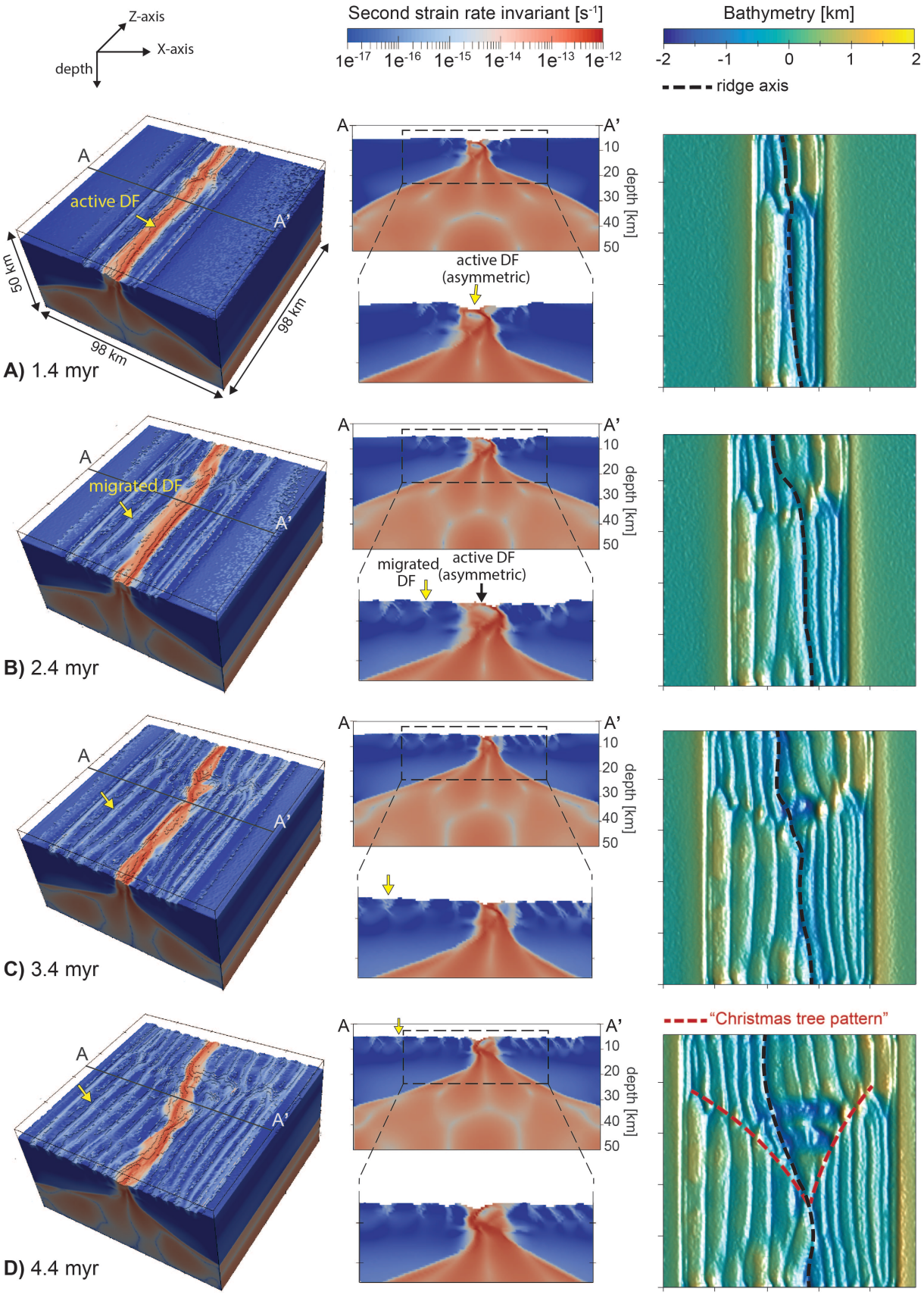
Z-axis
X-axis
depth
Second strain rate invariant [s-1]
1e-17 1e-16 1e-15 1e-14 1e-13 1e-12
Bathymetry [km]
-2 -1 0 1 2
ridge axis
A
A'
active DF
50 km
98 km
98 km
A) 1.4 myr
active DF
(asymmetric)
depth [km]
10
20
30
40
50
migrated DF
B) 2.4 myr
C) 3.4 myr
D) 4.4 myr
"Christmas tree pattern"

Figure 2 – Results of the evolution of the reference model *diaa* ($\dot{\varepsilon}_{healing}$ = 0 and C_0/C_1 = 10/3) during oceanic spreading. Strain rate (logarithmic scale) and topography are displayed. **(a)** Model results at t=1.4 Myr **(b)** Model results at t=2.4 Myr **(c)** Model results at 3.4 Myr **(d)** Model results at t=4.4 Myr, a ridge-oblique pattern has developed within the topography (right plot): "*Christmas Tree Pattern".* **DF** = detachment fault.

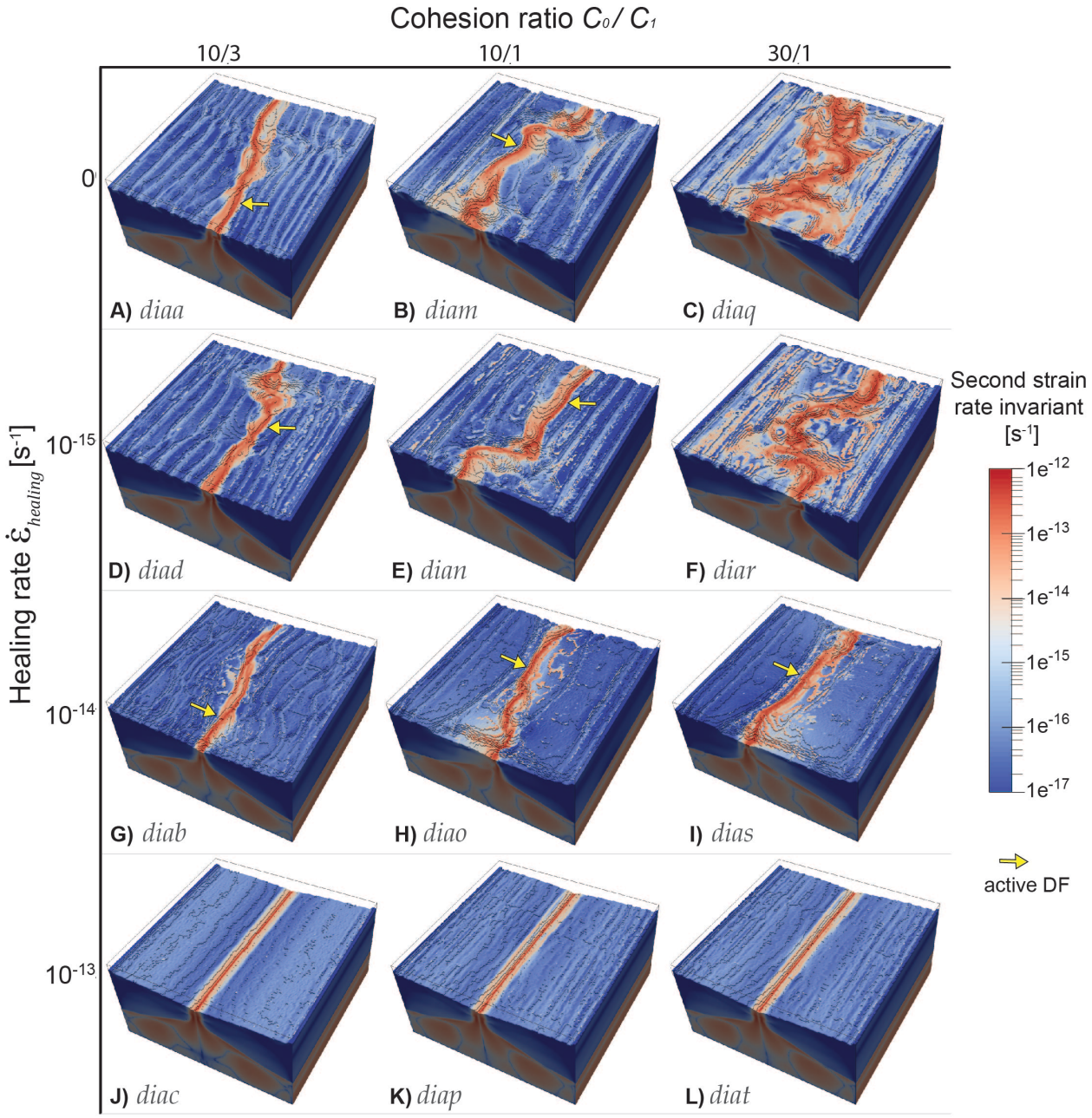

Figure 3 – Area diagram of 12 models varying in healing rate $\dot{\varepsilon}_{healing}$ and C_0/C_1 cohesion ratio values, showing their mature spreading patterns at 5 Myr. The second invariant of the strain rate (logarithmic scale) is displayed. The surface trace of the active detachment fault is marked by the yellow arrow. For models *diaq* **(c)** and *diar* **(f)**, the surface deformation pattern is too spread out to identify the surface trace of the active detachment fault.

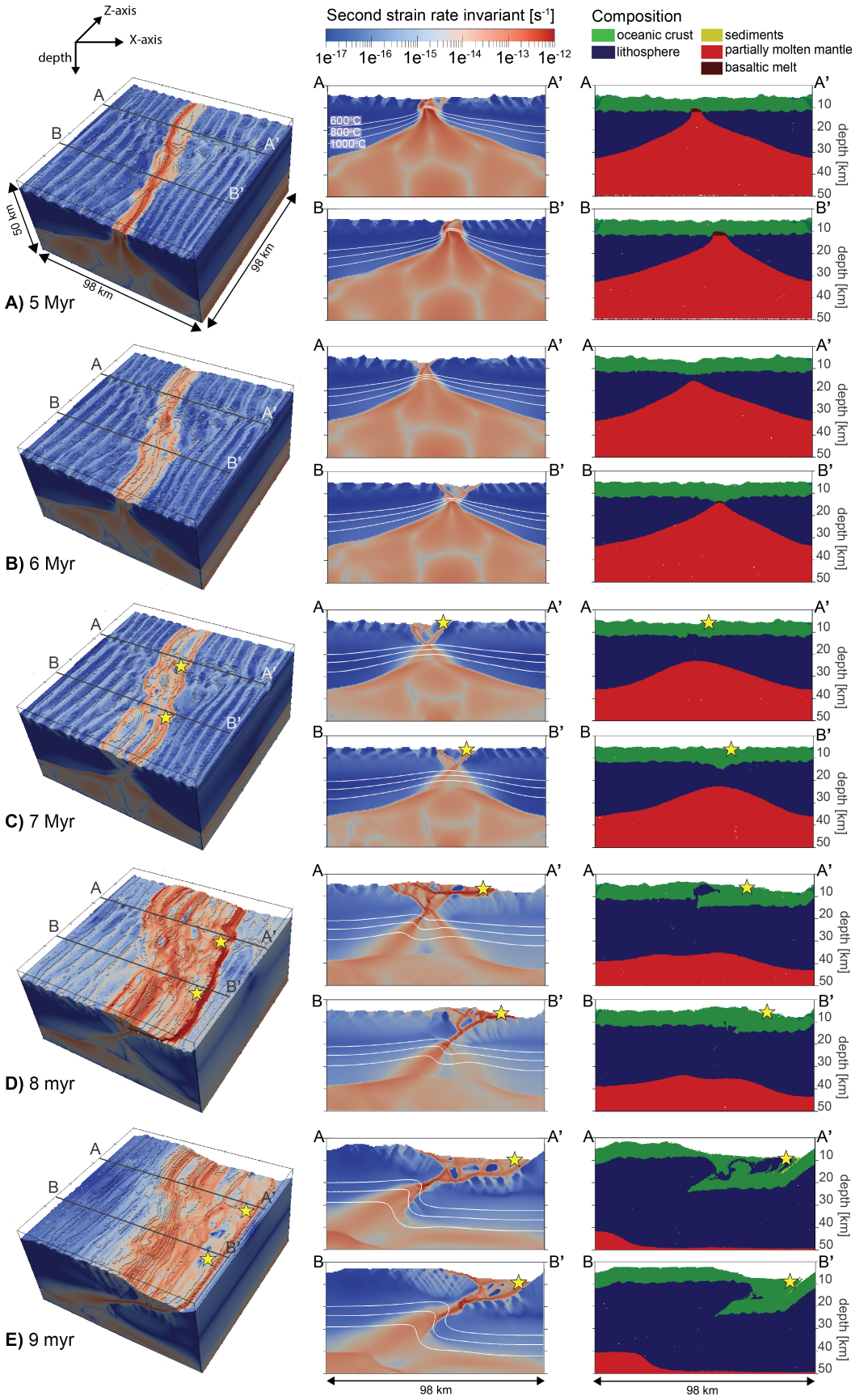
Z-axis
X-axis
depth
Second strain rate invariant [s-1]
1e-17 1e-16 1e-15 1e-14 1e-13 1e-12
Composition
oceanic crust
lithosphere
sediments
partially molten mantle
basaltic melt
600°C
800°C
1000°C
A
A'
B
B'
depth [km]
50 km
98 km
A) 5 Myr
B) 6 Myr
C) 7 Myr
D) 8 myr
E) 9 myr

Figure 4 – Results of the evolution of the reference model *diaa* ($\dot{\varepsilon}_{healing}$= 0 and C0/C1 = 10/3) during inversion from oceanic spreading to convergence. Strain rate (logarithmic scale) and composition are displayed, as well as the temperature isolines of 600, 800 and 1000°C. The yellow star denotes the onset of the underthrust. **(a)** Model results at t=5.0 Myr; **(b)** Model results at t=6.0 Myr; **(c)** Model results at 7.0 Myr; **(d)** Model results at t=8.0 Myr; **(e)** Model results at t=9.0 Myr, many detachment faults have interacted with one another forming an incipient accretionary wedge atop the underthrusted plate.

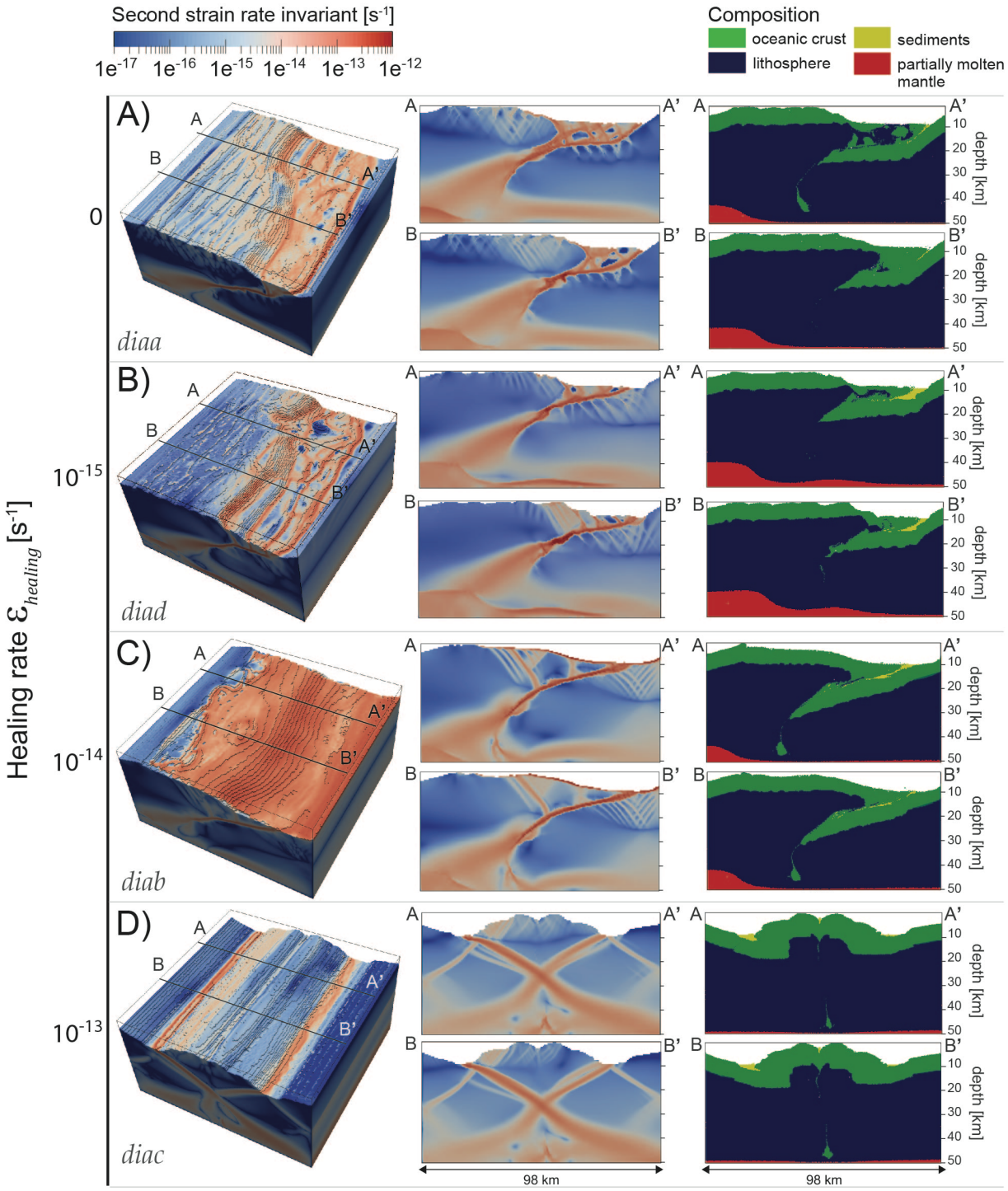

Figure 5 – Inversion results at time t=9.0 Myr for 4 models with different fracture healing rates. Strain rate (logarithmic scale) and composition are displayed. **(a-b)** Reference model *diaa* and model *diad* (inverted asymmetric spreading system which had many detachments running parallel to the ridge) show a stagnant underthrusted plate topped by many reactivated former detachment faults; **(c)** model *diab* (inverted asymmetric

spreading system without the presence of detachment faults) shows a downward plunging plate and **(d)** model *diad* (inverted symmetric spreading system) evolved in a symmetric pattern with two active conjugate thrusts on both side of the former spreading ridge.

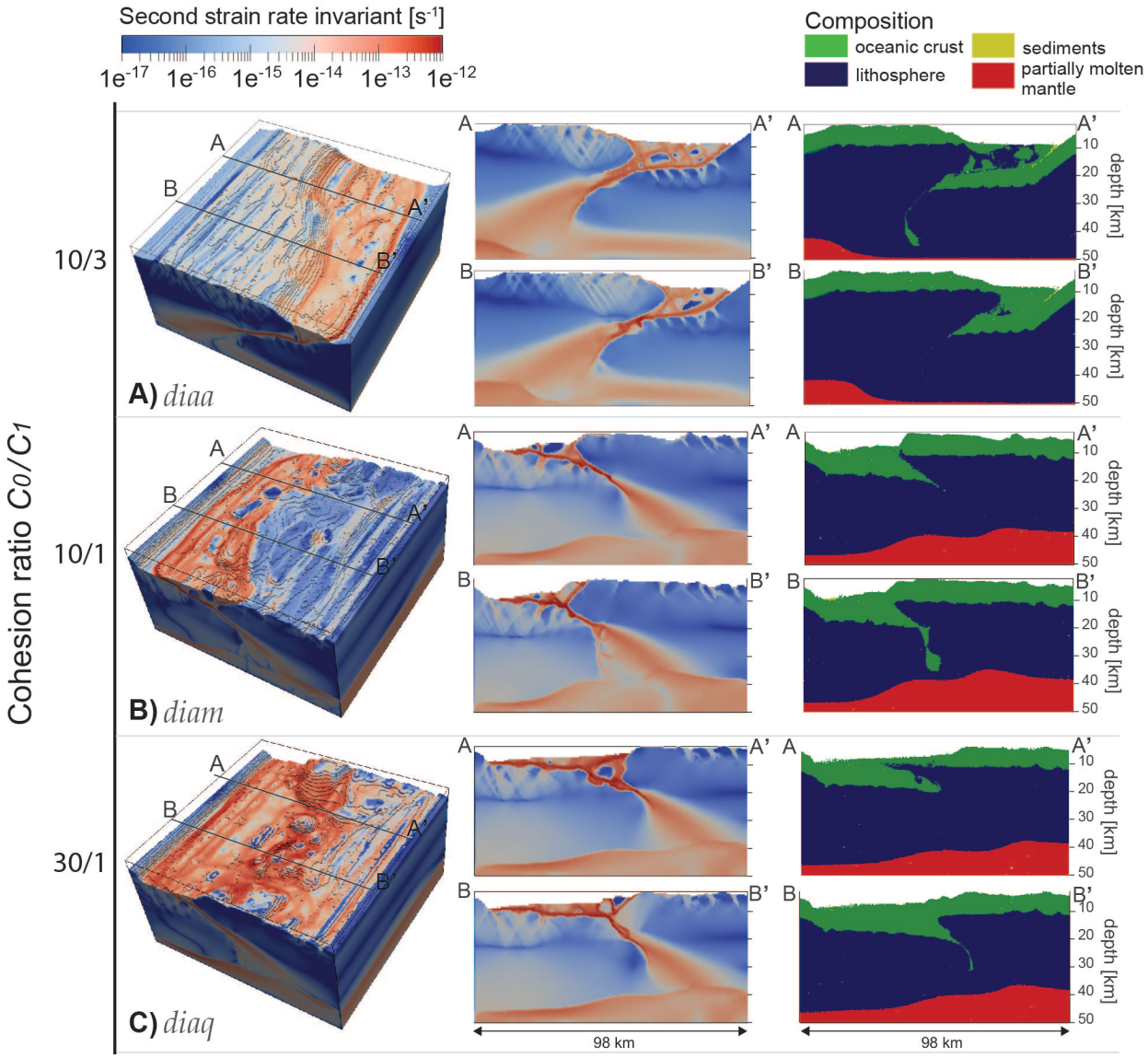

Figure 6 – Inversion results at time t=9.0 Myr for 3 models with different cohesion ratio, displaying the strain rate (logarithmic scale) and compositional slices. **(a)** Reference model *diaa*; **(b)** model *diam* and **(c)** model diaq (all inverted asymmetric spreading systems with the occurrence of ridge-parallel detachment faults). Inverted profiles show underthrusting of one plate along a major reverse fault. Increased cohesion ratios produce larger amount of localized deformation along the main thrust plane and a smaller accretionary wedge atop the fault.

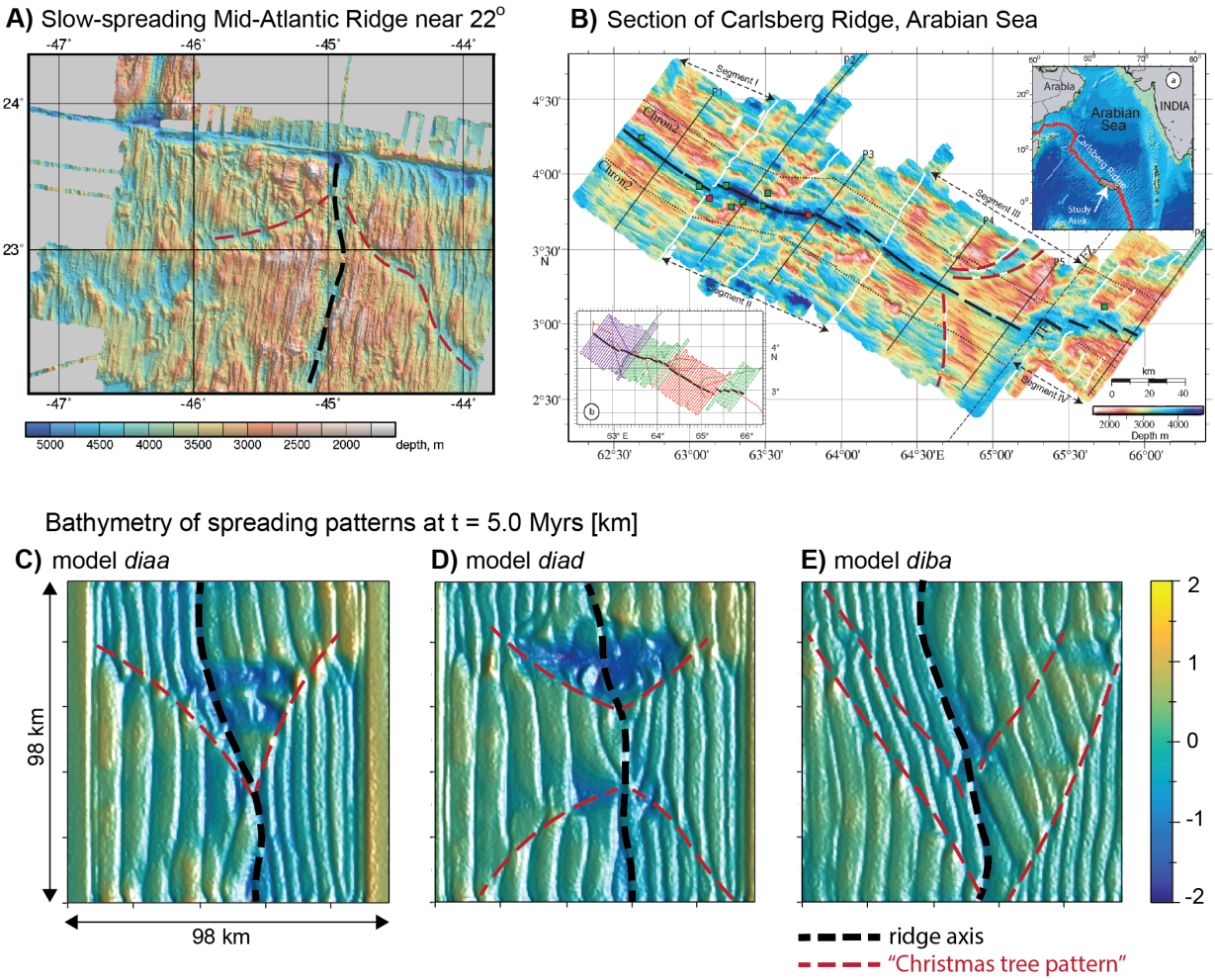

Figure 7 - Comparison between natural data and numerical models for the occurrence of "Christmas tree patterns". **(a)** Bathymetry of slow-spreading Mid-Atlantic Ridge near 22° (from McDuff and Heath, 2001); **(b)** Bathymetry of Carlsberg Ridge in the Arabian Sea (From Kattoju et al., 2015); **(c)** bathymetry of mature spreading pattern of model *diaa;* **(d)** bathymetry of mature spreading pattern of model *diad;* **(e)** bathymetry of mature spreading pattern of model *diba*.

Tables

Material	sediments	Oceanic crust	lithosphere	Partially molten mantle	Basaltic melt
η [Pa^n s] [a]	1.97E+17	4.90E+22	3.98E+16	3.98E+16	4.80E+16
E_a [J] [b]	1.54E+05	2.38E+05	5.32E+05	5.32E+05	2.38E+05
V_a [J/bar] [b]	0	0	1.6	0.8	0.8
σ_{crit} [Pa] [b]	3.00E+04	3.00E+04	3.00E+04	3.00E+04	3.00E+04
n [b]	2.30	3.20	3.50	3.50	3.20
C_o [Pa] [b]	1.00E+06	1.00E+07*	3.00E+06	3.00E+06	3.00E+06
C_1 [Pa] [b]	1.00E+06	3.00E+06*	3.00E+06	3.00E+06	3.00E+06
$\tan(\varphi_0)$ [b]	0.200	0.600	0.600	0	0
$\tan(\varphi_1)$ [b]	0.200	0	0	0	0
ε_o [b]	0.0	0.0	0.0	1.0	1.0
ε_1 [b]	1.0	1.0	1.0	1.0	1.0
ρ_o [kg/m^3] [b]	2600	3000	3300	2900	2800
α [K^{-1}] [b]	3.00E+05	3.00E-05	3.00E-05	3.00E-05	3.00E-05
κ [W/m/K] [a]	0.64	1.18	0.73	0.73	1.18
$\kappa_{koef}T$ [W/m] [a]	8.072E+02	4.74E+02	12.93E+02	12.93E+02	4.74+02
Ht [W/kg] [a]	2.00E-06	0.25E-06	2.20E-08	2.20E-08	0.25E-08

Table 1 – Material parameters used in the numerical experiments. From (a) Turcotte and Schubert (2002) and (b) Ranalli (1995). η: initial viscosity, E_a: activation energy, V_a: activation volume, σ_{crit}: diffusion-dislocation creep transition stress, n: exponent parameter, C_o & C_1: cohesion, $\tan(\varphi_0)$ & $\tan(\varphi_1)$: internal friction angles, ε_o & ε_1: strain weakening coefficients, ρ_o: initial density, α: thermal expansion, κ: thermal conductivity, $\kappa_{koef}T$: thermal conductivity temperature coefficient, Ht: radioactive heat production. * denotes that these material parameters are changed throughout the experiments. All materials were assigned the same values for compressibility: β=1.00E-03 kbar^{-1} and heat capacity: C_p= 1.00E+03 J/kg.

Sticky water: η=1.00E+18; n=1.00; ε_o - ε_1= 0.1-1.0; ρ_o= 1000; C_p = 3.30+03; κ= 200.

Sticky air: η=1.00E+18; n=1.00; ε_o - ε_1= 0.0-1.0; ρ_o= 1.00; C_p = 3.30+06; κ= 200.

Model	Spreading (and convergence) rate [cm/yr]	Healing rate [s^{-1}]	Cohesion ratio [MPa]	Mature spreading pattern	Inversion time (t_{init}-t_{end}) [Myr]	Inversion results
diaa	1.9	0	10/3	Asymmetrical accretion, curved ridge, many ridge-parallel DF, abyssal hills and lows	5-8	Underthrusting plane along lower ends DF, accretionary wedge with BT
diax	1.9	0	10/3		5-10	Underthrusting plane along lower ends DF, accretionary wedge with BT
diad	1.9	10E-15	10/3	Asymmetrical accretion, curved ridge, many ridge-parallel DF, abyssal hills and lows	5-8	Underthrusting plane along lower ends DF, accretionary wedge with BT
diab	1.9	10E-14	10/3	Slightly curved ridge, ridge-parallel rugged topography, no preservation DF	5-8	Underthrusting, no accretionary wedge or BT
diay	1.9	10E-14	10/3		5-10	Underthrusting, no accretionary wedge or BT
diac	1.9	10E-13	10/3	Symmetrical pattern, straight ridge, smooth topography	5-8	Symmetrical response: no underthrusting, symmetrical ridge swell
diam	1.9	0	10/1	Asymmetrical accretion, curved ridge with TO, many ridge-parallel DF	5-8	Underthrusting plane along lower ends DF, accretionary wedge with mesh of deformation
dian	1.9	10E-15	10/1	Asymmetrical accretion, curved ridge with TO, many ridge-parallel DF	5-8	Underthrusting plane along lower ends DF, accretionary wedge with mesh of deformation
diao	1.9	10E-14	10/1	Slightly curved ridge, ridge-parallel rugged topography, no preservation DF		
diap	1.9	10E-13	10/1	Symmetrical pattern, straight ridge, smooth topography		
diaq	1.9	0	30/1	Very curved ridge segmented by TO, ridge-parallel DF	5-8	Underthrusting plane along lower ends DF, accretionary wedge with mesh of strain localization
diar	1.9	10E-15	30/1	Very curved ridge segmented by TO, ridge-parallel DF	5-8	Underthrusting plane along lower ends DF, accretionary wedge with mesh of deformation
dias	1.9	10E-14	30/1	Slightly asymmetrical accretion, straight ridge, ridge-parallel rugged topography		
diat	1.9	10E-13	30/1	Symmetrical pattern, straight ridge, smooth topography		
diba	2.5	0	10/3	Curved ridge, many ridge-parallel DF, abyssal hills and lows	5-8	Underthrusting plane along lower ends DF, accretionary wedge with BT
dibb	2.5	10E-14	10/3	Slightly curved ridge, ridge-parallel rugged topography	5-8	Underthrusting, no accretionary wedge or BT
diea	1.5	0	10/3	Asymmetrical accretion, curved ridge, many ridge-parallel DF, abyssal hills and lows	5-8	Underthrusting plane along lower ends DF, accretionary wedge with BT

Table 2 – Conditions, mature spreading pattern results and inversion results of numerical experiments. The Nusselt number was set to 2.0 for all models. DF = detachment faults; TO= transformal offsets; BT = back-thrusts.